

Article

Preparation, Microstructural Characterization and Photocatalysis Tests of V⁵⁺-Doped TiO₂/WO₃ Nanocomposites Supported on Electrospun Membranes

Michel F. G. Pereira¹, Mayane M. Nascimento¹, Pedro Henrique N. Cardoso¹, Carlos Yure B. Oliveira² ,
Ginetton F. Tavares³  and Evando S. Araújo^{1,*} 

¹ Research Group on Electrospinning and Nanotechnology Applications (GPEA-Nano), Department of Materials Science, Federal University of San Francisco Valley, Juazeiro 48902-300, Brazil

² Department of Fishing and Aquaculture, Federal Rural University of Pernambuco, Recife 52171-900, Brazil

³ Research and Extension Center, Laboratory of Fuels and Materials (NPE/LACOM), Department of Chemistry, Federal University of Paraíba, Campus I, João Pessoa 58051-900, Brazil

* Correspondence: evando.araujo@univasf.edu.br; Tel.: +55-74-2102-7645

Abstract: Metal oxide nanocomposites (MON) have gained significant attention in the literature for the possibility of improving the optical and electronic properties of the hybrid material, compared to its pristine constituent oxides. These superior properties have been observed for TiO₂ — based MON, which exhibit improved structural stability and photoactivity in environmental decontamination processes. In addition, the use of polymer membrane-supported MON is preferable to prevent further aggregation of particles, increase the surface area of the semiconductor in contact with the contaminant, and enable material reuse without considerable efficiency loss. In this work, V⁵⁺-doped TiO₂/WO₃ MON nanostructures were prepared by the sintering process at 500 °C and supported in electrospun fiber membranes for application as photocatalyst devices. Microstructural characterization of the samples was performed by XRD, SEM, EDS, Raman, and DSC techniques. The reflectance spectra showed that the bandgap of the MON was progressively decreased (3.20 to 2.11 eV) with the V⁵⁺ ions doping level increase. The fiber-supported MON showed photoactivity for rhodamine B dye degradation using visible light. In addition, the highest photodegradation efficiency was noted for the systems with 5 wt% vanadium oxide dispersed in the fibers (92% dye degradation in 120 min of exposure to the light source), with recyclability of the composite material for use in new photocatalysis cycles. The best results are directly related to the microstructure, lower bandgap and aggregation of metal oxide nanocomposite in the electrospun membrane, compared to the support-free MON.

Keywords: metal oxide nanocomposites; microstructural analysis; electrospinning; polymer substrate; photodegradation



Citation: Pereira, M.F.G.; Nascimento, M.M.; Cardoso, P.H.N.; Oliveira, C.Y.B.; Tavares, G.F.; Araújo, E.S. Preparation, Microstructural Characterization and Photocatalysis Tests of V⁵⁺-Doped TiO₂/WO₃ Nanocomposites Supported on Electrospun Membranes. *Inorganics* **2022**, *10*, 143. <https://doi.org/10.3390/inorganics10090143>

Academic Editor: Roberto Nisticò

Received: 2 August 2022

Accepted: 14 September 2022

Published: 19 September 2022

Publisher's Note: MDPI stays neutral with regard to jurisdictional claims in published maps and institutional affiliations.



Copyright: © 2022 by the authors. Licensee MDPI, Basel, Switzerland. This article is an open access article distributed under the terms and conditions of the Creative Commons Attribution (CC BY) license (<https://creativecommons.org/licenses/by/4.0/>).

1. Introduction

The increase in industrial activity associated with the accelerated growth of the world population in recent decades is one of the main factors that contribute to the pollution of the physical and biological components on earth. In particular, the inappropriate disposal of by-products from the production of medicines, agrochemicals, heavy metals, and dyes can contaminate aquatic environments, due to its toxic and carcinogenic components resulting from the decomposition of its molecules. The scarcity of effective and low-cost procedures that ensure large-scale discarding and treatment of industrial waste contributes to intensifying this current problem [1,2].

Although the advanced water treatment technologies, such as sedimentation, coagulation, aerobic-activated sludge-based treatment, and nitrification–denitrification have been widely used after conventional primary and secondary treatments, they have some

drawbacks, such as high energy consumption, carbon emission, excess sludge discharge, ineffectiveness in removing contaminants, such as organic dyes, and considerable additional cost [3,4]. In this sense, the search for new technologies and functional materials for water treatment that are able to meet current needs, with lower cost and environmental impact, is an open field of research today [2,5–7].

Metal oxides (semiconductors that respond to external stimulus—light, electric potential, pressure, among others) have received increased attention from academic researchers and industrial developers as potential materials for the production of efficient and environmentally friendly devices for the remediation of organic-contaminated water [8–10]. This ability is directly related to their intrinsic properties, such as high chemical and structural stability, high surface area/volume ratio, excellent electrical/electronic response, surface interactions with contaminant molecules, and the possibility of reusing the material in new decontamination cycles [8].

In particular, the use of metal oxide nanocomposites (MON) (resulting from the mixture between two or more selective nanoscale metal oxides [11,12]) has been preferable for these applications, due to the possibility of having better decontamination performance when compared to the use of their constituent oxides, in isolation. Currently, among the environmentally friendly techniques for removing contaminants using MON, heterogeneous photocatalysis (HP) stands out [13,14].

Heterogeneous photocatalysis is a photochemical process for the formation of free radicals, such as the hydroxyl $\text{HO}\cdot$, which is a highly oxidizing agent, and degrades organic substances present in water. When the semiconductor in solution is exposed to a light source with sufficient energy to activate it, the absorption of photons with higher energy than the semiconductor bandgap occurs. At the electronic level, this process causes an electron (e^-) to be transferred from the valence band to the conduction band of the material, leaving a hole (h^+) in the valence band. These holes generate $\text{HO}\cdot$ free radicals from the water adsorbed on the metal oxide surface, which are used in the organic contaminant oxidation reactions [14].

Titanium dioxide in its allotropic anatase form (anatase TiO_2 , ~3.2 eV bandgap) is one of the most widely used oxides in HP using MON, due to its non-toxicity, high chemical stability, excellent photoactivity and photostability, and lower cost than other oxides [15,16]. A limitation for photocatalytic processes using anatase is the demand of ultraviolet radiation as a light stimulus. The light source must have a higher energy than the material bandgap energy, so that electrons from its valence band can be ejected into its conduction band, which would not occur using visible light. Advances in this field of research involve the incorporation of selective metal oxides into TiO_2 , such as tungsten, zinc, indium, copper, niobium, and vanadium oxides, in order to increase the process efficiency [1,15,17,18].

Tungsten trioxide (WO_3 , 2.6–2.8 eV bandgap) has excellent electrical charge transfer properties, broadens the excitation wavelength range of the final material, in addition to promoting effective photocharge separation of the composite catalyst and inhibiting electron-hole recombination, which significantly improves the MON photocatalytic activity [19,20]. The interaction of WO_3 with TiO_2 increases the conductivity of the TiO_2/WO_3 system in comparison to pure TiO_2 [21,22], while TiO_2 doping with niobium pentoxide (Nb_2O_5) [23] or vanadium pentoxide (V_2O_5) [24] delays the phase transition from anatase to rutile (phase with less active surface) and improves the electronic properties of the resulting material [17]. In addition, the combined action between TiO_2 , WO_3 , and V_2O_5 results in nanocomposites with superior performance (sensitivity, electric and electronic properties, catalysis and phase stability), which demonstrate the emerging possibilities of using this MON configuration for environmental decontamination applications [21,25,26].

Its particles must be available in a small enough size to provide a large surface area of action, in order to enhance the MON photocatalytic activity. In practice, as the concentration of nanoparticles in solution increases, the tendency of these particles to agglomerate can also increase [27], which is the opposite of what is expected. In these studies, the impossibility of filtration or complete removal of oxide particles from the

aqueous environment after the reaction is observed. This represents a limitation for the reuse of the functional material in new photocatalysis cycles (or even to prevent water contamination) [28]. In recent years, these limitations have motivated the development of supported nanoparticles [29,30]. In this configuration, different types of substrates are used, such as porous glasses, lamellar compounds, zeolites, and polymer membranes, in order to disperse and stabilize the metal oxides [29,30]. The advantages of using an inert polymeric matrix as support for photocatalysts are the possibility of having flexible devices, as well as the ease of oxides removal from the aqueous environment, without significant loss of photocatalyst for reuse [29,31].

In this work, V^{5+} -doped TiO_2/WO_3 (1/1 in mol) nanostructures were prepared with different dopant concentrations, dispersed in a fibrous membrane (with high surface area to volume ratio) from the electrospinning process and tested as photocatalyst device. The materials microstructure was characterized by scanning electron microscopy (SEM), energy dispersive spectroscopy (EDS), X-ray diffraction (XRD), Raman spectroscopy, differential scanning calorimetry (DSC), and UV-vis with diffuse reflectance spectroscopy (DRS) methods, and their properties were related to the results obtained in photocatalysis tests, from the degradation of rhodamine B (RhB) model dye in aqueous solution. The results indicated that the interaction between the constituent oxides and their dispersion in the electrospun membrane were factors that significantly improved the efficiency of the degradation process using visible light, in addition to enabling the reuse of these functional materials in new photocatalysis cycles.

2. Results and Discussion

2.1. Microstructural Analysis

The XRD data of the TW, TWV3, and TWV5 MON are shown in Figure 1. The X-Pert HighScore software was used to identify the crystal phases of the studied materials. The crystallographic parameters were obtained from the International Center for Diffraction Data (ICDD). The tetragonal crystal phase of the anatase TiO_2 ($a = b = 3.7821 \text{ \AA}$, $c = 9.5022 \text{ \AA}$, and $\alpha = \beta = \gamma = 90^\circ$ lattice constants [32], 01-071-1166 ICDD card) and monoclinic WO_3 ($a = 7.306 \text{ \AA}$, $b = 7.540 \text{ \AA}$, $c = 7.692 \text{ \AA}$, $\alpha = \gamma = 90^\circ$ and $\beta \neq 90^\circ$ [33], 01-083-0951 ICDD card) were detected by XRD measurements. This demonstrates that the oxide mixture sintering (with the selected parameters) has not resulted in a phase change or crystalline solid solution formation in the resulting MON.

In addition, no diffraction peaks of V_2O_5 were detected in the XRD spectra of the TWV3 and TWV5 composites, in comparison to the TW sample [34]. The V_2O_5 nanopowders were used with low weight percentages and are uniformly dispersed in the TiO_2/WO_3 base mixture. This corroborates that the crystallographic planes of V_2O_5 (concentrated in the region of $2\theta = 20\text{--}35^\circ$ [35]) were superimposed by the peaks of TiO_2 and WO_3 (with higher intensities).

All sintered oxide mixtures show similar values of WO_3 parameters, with $a = 7.30 \text{ \AA}$, $b = 7.53 \text{ \AA}$, $c = 7.68 \text{ \AA}$, $\alpha = \gamma = 90^\circ$, and $\beta = 90.59^\circ$, with no changes in comparison to lattice constants of the starting material.

The TiO_2 crystal constants in the TW sample (Table 1) also show similar results to the pristine material ($a = b = 3.783 \text{ \AA}$, $c = 9.509 \text{ \AA}$, and $\alpha = \beta = \gamma = 90^\circ$ [22]), since the 1:1 in mol $TiO_2:WO_3$ configuration (WO_3 wt% close to that of TiO_2) provides a greater surface interaction between the oxides [34]. On the other hand, the a , b , and c values increased in vanadium-doped samples, in comparison to the TW sample (Table 1). This also demonstrates an increase in the TiO_2 unit cell volume (with no significant difference in this variable from TWV3 to the TWV5 sample). This suggests an atomic interaction degree, directly proportional to the dopant concentration. In fact, the ionic radius of the V^{5+} ions (0.68 \AA [36]) is approximate to the T^{4+} ions, which step up the occurrence of vanadium ions doping in the atomic structure of anatase, because of the sintering process.

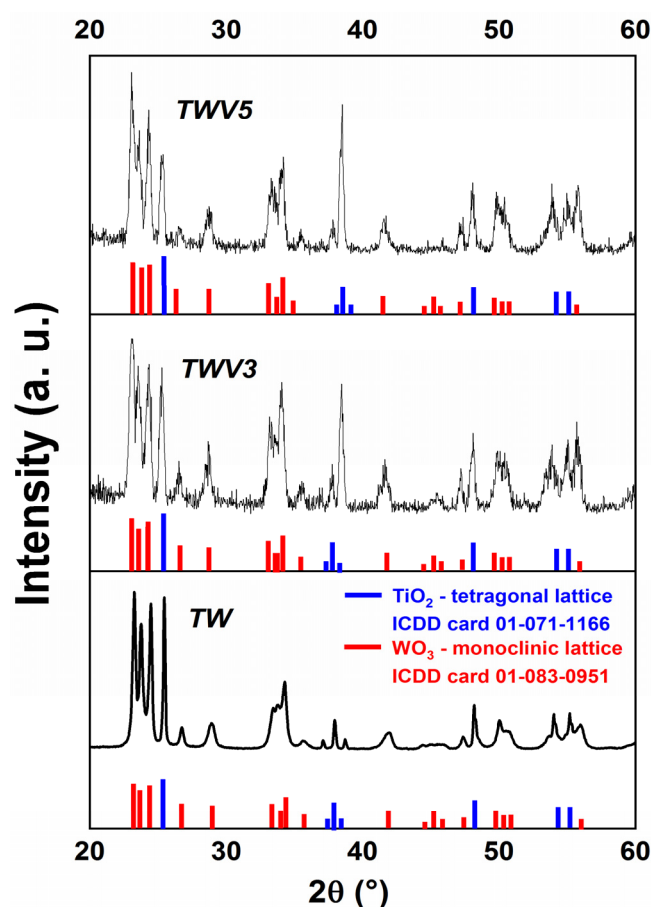


Figure 1. XRD spectra of the TW, TWV3 and TWV5 nanostructures. The colored bars represent the crystallographic planes described in the TiO_2 and WO_3 ICDD cards.

Table 1. Lattice constants and crystallite size of titanium dioxide in TW, TWV3, and TWV5 MON.

MON	Lattice Parameters (Å)		Average Crystallite Size, D (nm)
	a = b	c	
TW	3.783	9.509	20.23 (± 2.09)
TWV3	3.803	9.704	25.31 (± 2.64)
TWV5	3.804	9.708	25.43 (± 2.67)

The crystallite average sizes (D) of the WO_3 and TiO_2 in the sintered MON were calculated by the modified Scherrer equation (MSE). By the equation, $D = \lambda / (3\beta \cos(\theta))$ [37], where λ is the wavelength of X-ray radiation, β is the width at half height of the peaks detected in the XRD spectrum, θ is the half of the diffraction angle in these crystallographic planes, and 1/3 is the correction factor for the limit of application of the Scherrer law [38].

The WO_3 presented D values of 15.67 (± 1.22) nm, 15.84 (± 1.04) nm, and 15.91 (± 1.62) nm for the TW, TWV3, and TWV5 samples, respectively. In addition, in these systems, the crystallite size values for TiO_2 (Table 1) were 20.23 (± 2.09) nm, 25.31 (± 2.64) nm, and 25.43 (± 2.67) nm, in increasing order of V_2O_5 concentration.

The results for the hypothesis test of means equality ($n = 3$) demonstrated that the average size of the WO_3 crystallite does not indicate significant changes in the three MON configurations. On the other hand, in MON doped with 3 wt% and 5 wt% of vanadium oxide, a significant increase in TiO_2 crystallite size is confirmed when compared to the TW sample. There is no statistical difference between the D values calculated for these last two systems.

The Raman spectra of MON are presented in Figure 2. The spectrum of pristine anatase TiO_2 was also analyzed in order to compare with composite samples. In Figure 2a is shown that the molecular vibration bands of anatase (141, 196, 397, 514, and 638 cm^{-1} wavenumbers [39]) occur in all spectra of the metal oxide nanocomposites, although shifted to lower wavenumbers (redshift), by $7\text{--}11\text{ cm}^{-1}$. In addition, the monoclinic WO_3 bands were determined, typically at 268, 319, 710, and 802 cm^{-1} , with no wavenumber variation in comparison to the pure oxide [34,40].

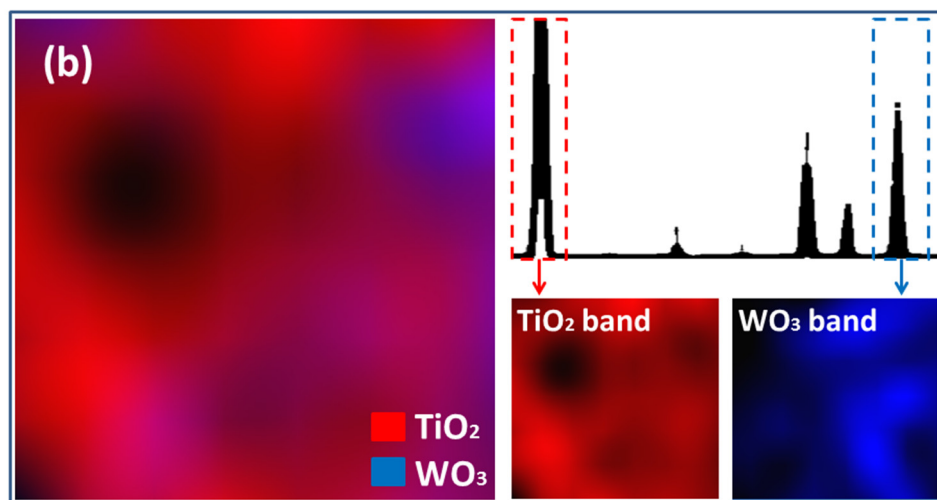
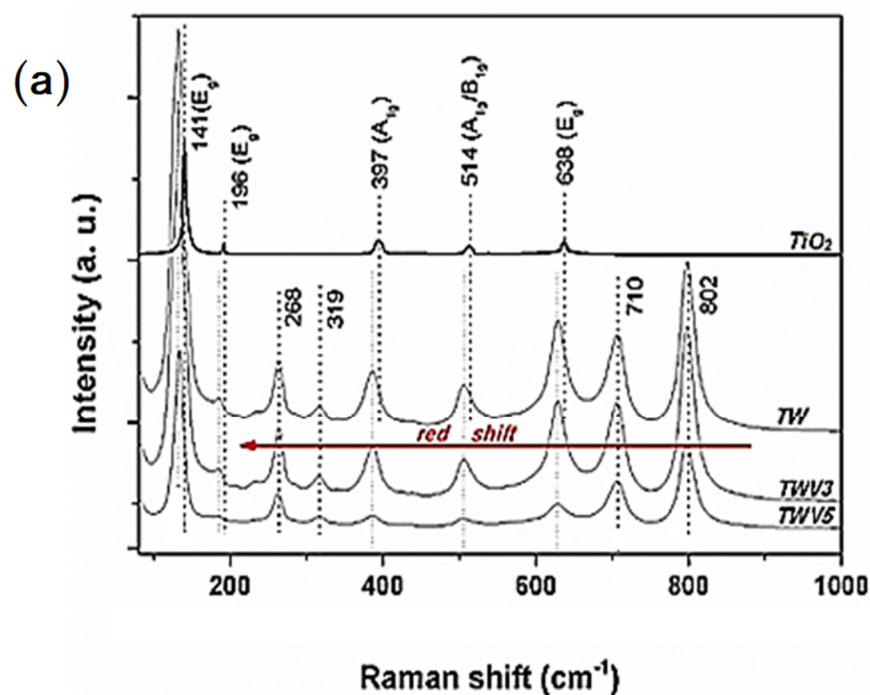


Figure 2. (a) Raman spectra of the metal oxide nanocomposites compared to pristine anatase TiO_2 ; (b) representative Raman mapping of MON samples, with indication of TiO_2 and WO_3 vibrational bands.

The redshift effect occurs due to the process of surface relaxation, distortions, and additional vibration energy in the crystal lattice (phonon confinement) of the material [41]. In particular, the occurrence of this phenomenon in the MON Raman spectra indicates that W^{6+} and V^{5+} ions occupied vacancies of available Ti atoms in the crystal lattice of anatase (as previously expected). The occupation of these sites by W and V species allows

a greater degree of local vibrations and facilitates the molecules collective excitation, which favors photocatalysis processes [41,42]. The representative Raman mapping (Figure 2b) of V^{5+} -doped samples is an important tool that confirms the regular distribution of TiO_2 and WO_3 bands in the materials surface, with no additional active vibration modes in these MON.

The combined results of SEM images, XRD (with anatase unit cell volume invariance in V^{5+} -doped MON), and Raman analysis (not detected V_2O_5 bands, with redshift of TiO_2 bands) indicate that at 5 wt% dopant concentration, a greater amount of the vanadium species is arranged in the sites initially unoccupied by titanium atoms, showing the effectiveness of the performed doping process.

The study of variations in crystallite sizes in the nanostructured systems was important to determine the doping level in the atomic structure of TiO_2 and their effects for application of these materials as photocatalysts. In fact, when the MON crystallites are in nanometer scale, the movement of electrons and holes in an excited semiconductor also depends on the quantum confinement effect. In other words, the phonons resulting from the doping process also influence material electronic properties [43].

Surface micrographs of TWV3 and TWV5 MON (resulting from sintering at 500 °C) were obtained by SEM (Figure 3a,b). Initial analysis returns mostly spherical particles (100–230 nm range), with significant overall contact surface, with no significant differences when compared to the dopant-free TW matrix [22]. The EDS mapping of V^{5+} -doped samples (Figure 3c) confirms the Ti and W metals matrix and vanadium dopant evenly distributed over the entire material structure, which favors the application of these nanostructures as photocatalysts.

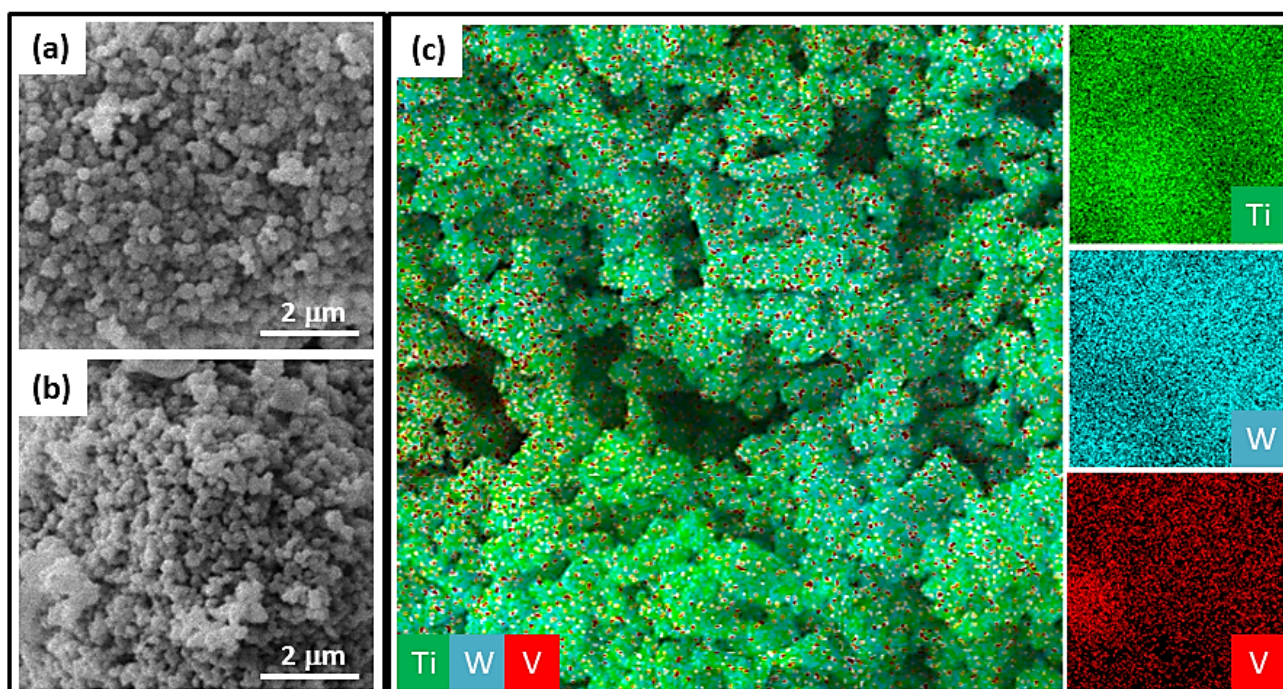


Figure 3. SEM micrographs of (a) TWV3 and (b) sintered TWV5 MON; (c) representative EDS mapping of V^{5+} -doped samples, with indication of Ti, W, and V elements.

The calculated mean sample diameters were 145.7 ± 47.0 nm ($n = 135$) [20], 160.1 ± 74.1 nm ($n = 123$), and 169.4 ± 63.1 nm ($n = 141$), for TW, TWV3, and TWV5 MON, respectively. The equality of means tests results ($n = 3$) demonstrate that there is no significant difference between the average particle size calculated for these produced MON (p -value $> \alpha$ for all comparison of means).

The bandgap energy of the MON semiconductors was calculated from the DRS data (Figure 4a), using the Tauc plot (Figure 4b). By the Tauc relation, the curve of the product of the absorption coefficient (α) and photon energy ($E = h\nu$) to the power of $1/r$, $(\alpha h\nu)^{1/r}$, is plotted as a function of the photon energy (E). The intersection of the auxiliary line in the linearity region of the graph with the x axis represents the measurement of the material optical energy gap (E_g) [44]. Thus, the type of electronic transition (direct or indirect electron mobility from the valence to the conduction band) in a semiconductor is defined by the r value (equal to $1/2$ or 2 , for direct or indirect bandgap materials, respectively).

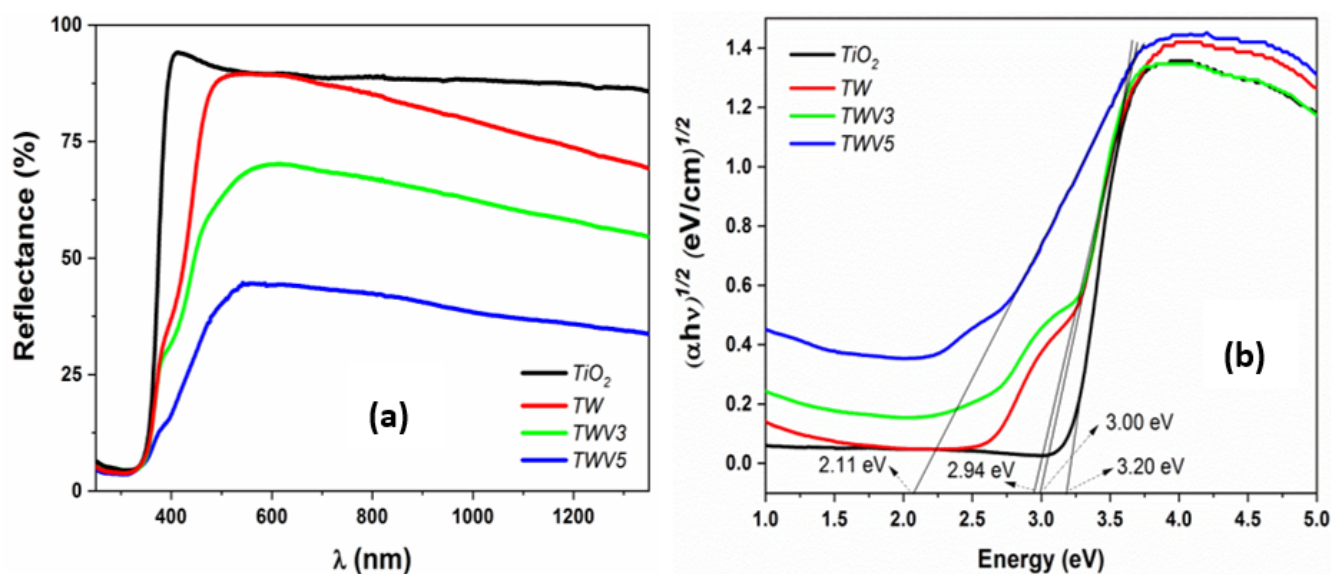


Figure 4. (a) DRS data and (b) Tauc plot for bandgap measurements of the nanostructured metal oxides.

The diffuse reflectance data of all tested nanostructures were modeled by the Tauc relation with $r = 2$, which indicates that the semiconductor excitation occurs by indirect transition. In other words, for our nanostructured systems, the electrons can be excited from the highest energy state in the valence band to the lowest level in the conduction band, with different momentum values. In this configuration, the electron mobility is facilitated by phonon assistance, which was detected and discussed for the MON samples in the Raman characterization.

The E_g experimental values of the hybrid semiconductors were progressively decreased with the V^{5+} doping level increase (gap energies estimated at 3.00, 2.94 and 2.11 eV for TW, TWV3, and TWV5 samples, respectively), compared to the pristine TiO_2 (a typical indirect bandgap semiconductor [44], with $E_g = 3.2$ eV).

As verified, the progressive introduction of vanadium oxide to the TiO_2/WO_3 mixture (1/1 in mol) significantly decreased the TiO_2 bandgap (3.20 eV to 2.11 eV). It is known that the presence of dopant ions in the system generates an extrinsic-type semiconductor (in which the bandgap can be controlled by purposefully adding impurities to the materials atomic structure).

In the case of our nanostructures, the TiO_2 (with tetravalent metal) is doped with V^{5+} ions (pentavalent elements), which will result in an n-type extrinsic semiconductor. In this case, free electrons are the main charge carriers, since each V^{5+} ion provides an additional electron to the system and thus the total number of electrons becomes greater than the number of holes. In this configuration, the added electrons tend to occupy additional energy levels in the bandgap region, very close to the bottom of conduction band (CB), called donor energy levels. Thus, it can be proposed from our results that the progressive increase in the concentration of vanadium in the nanostructures promoted a significant increase in the doping degree, with additional donor levels, which explains the decrease in the TiO_2 bandgap to 2.11 eV in the TWV5 nanocomposite.

In this sense, for the TWV5 system (with lower indirect bandgap), the electronic transition occurs with a lower photon energy linear, which makes it difficult for electron/hole recombination to occur, and consequently favors photocatalysis processes with visible light.

The SEM images and EDS analysis of the MON-loaded fibers are shown in Figure 5. It is noted that there is a predominance of regular diameter fibers, without apparent surface defects, which proves that the parameters of the electrospinning process were properly chosen for the production of TWV3- and TWV5-loaded electrospun membranes (Figure 5a,b).

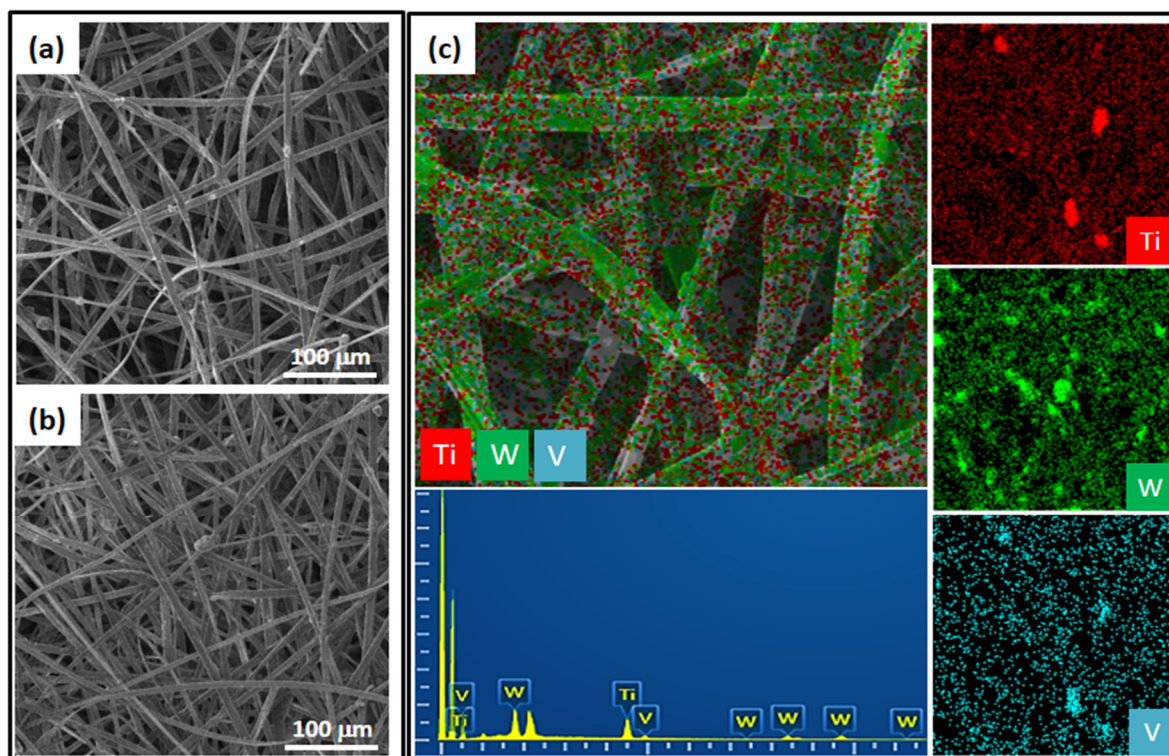


Figure 5. SEM micrographs of (a) TWV3 and (b) TWV5 MON-loaded electrospun fibers; (c) EDS mapping and elemental composition of V^{5+} -doped samples, with indication of Ti, W, and V elements.

The mean diameters of composite fibers were estimated as $5.4 \pm 1.7 \mu\text{m}$ ($n = 59$) [22], $5.8 \pm 2.3 \mu\text{m}$ ($n = 73$), and $6.0 \pm 1.9 \mu\text{m}$ ($n = 69$), with a progressive increase in V_2O_5 concentration. The population mean difference tests revealed that the MMO-loaded fibers have statistically similar mean diameters ($n = 3$ samples, p -value $> \alpha$).

The EDS mapping and elemental composition of these composite fibers (Figure 5c) confirmed that the Ti, W, and V elements are distributed throughout the fibrous polymer membrane. In other words, the electrospun fiber matrix promotes the dispersion of oxides, reducing the particle aggregation.

Thus, photocatalytic devices can be produced with better performance, due to the greater surface contact area of the MON, with the contaminated aqueous solution. In addition, the immobilization of MON in fibrous template allows the composite material reuse (without considerable material loss) in other photocatalysis cycles. Thus, electrospinning proves to be an effective and low-cost technique for producing potential composites for application in the decontamination of aqueous environments.

In summary, the similarity in morphology (particle size and fiber diameter) with increasing dopant concentration indicates that the better performance of these structures as a photocatalyst should predominantly refer to the interaction degree between the constituent oxides.

The DSC curves of the pristine fibrous membrane and the MON-loaded polymer fibers are given in Figure 6. In MON samples, two broad endotherm peaks are observed in the analyzed temperature range. The first one (centered at 75–90 °C) is assigned to the loss of water and the solvent remaining evaporation from the polymer electrospinning process [45,46].

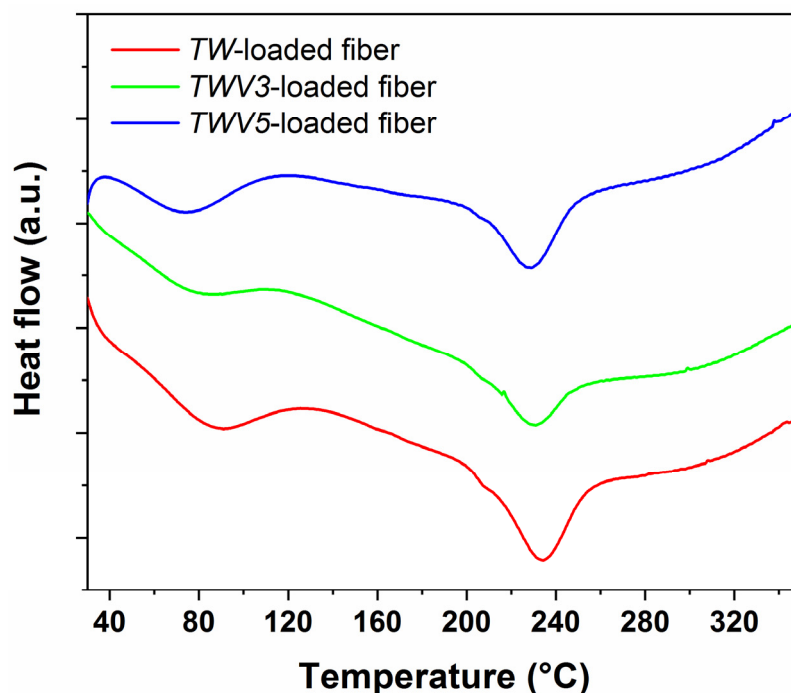


Figure 6. DSC curves of MON-supported fibers.

The second peak, centered at 231–234 °C, is related to the melting point of the polymer crystalline phase [46]. This peak is also described in the literature as the relaxation temperature of the polymer chains that follows the glass transition [47].

In addition, the transition temperatures for the constituent oxides are detected at higher temperatures than those observed in the experiment. In resume, the introduction of semiconductors preserves the polymer melting point, without significant changes in the homogeneity and crystallinity degree of the composites.

2.2. Photocatalysis Tests

During the experiment, aliquots of the RhB solution were removed from the reactor at defined time intervals so that variations in the intensity of the dye absorption peak (at $\lambda = 555$ nm) (Figure 7a–c) could be investigated. The photodegradation kinetic curves of Rhodamine B (RhB) dye using MON-loaded fibers, under visible light excitation, are demonstrated in Figure 7d. In the graph, the y-axis represents the change in the relative concentration (C/C_0) of the dye, where C_0 is the initial concentration and C is the remaining concentration of the contaminant in the reactor (as a function of time). All samples were preserved in a dark environment in contact with the dye in solution for 1 h before exciting the oxides with continuous radiation.

The use of the fibrous membrane (without additives) in solution returned negligible variation in the initial concentration of RhB ($1 \mu\text{M}$) throughout the analyzed time interval. This proves that the polymer matrix acts as an inert support to prevent the particle aggregation, and provides a greater oxides surface area to interact with the contaminant.

The pristine TiO_2 nanopowder was used in the experimentation and has not demonstrated considerable photocatalytic action in visible light, since the energy of the incident light photons was not sufficient to overcome the anatase bandgap energy (3.2 eV) and promote electron/hole mobility, which is necessary for the dye degradation process to occur.

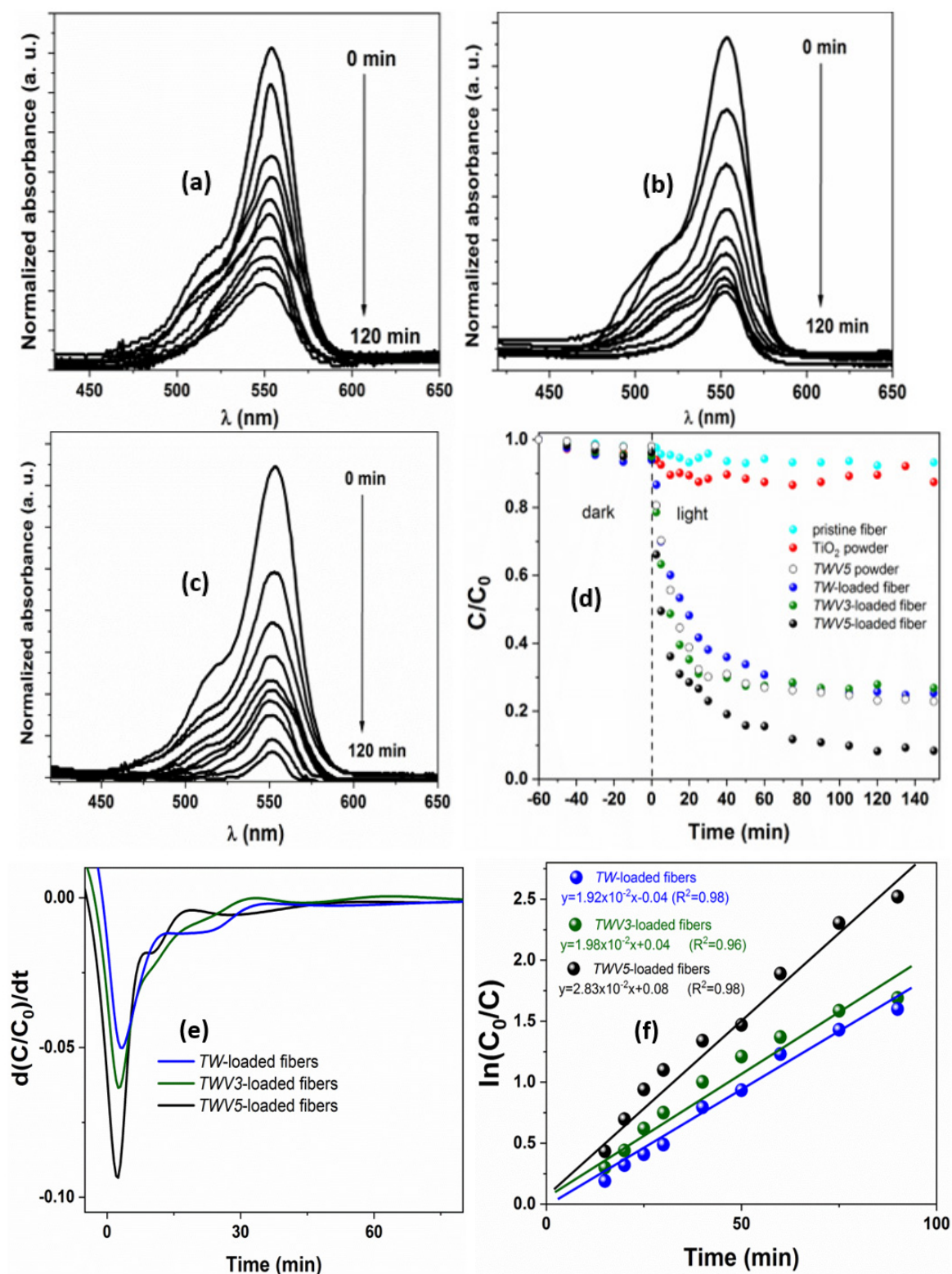


Figure 7. Change in absorbance spectra of RhB dye, using (a) TW-, (b) TWV3- and (c) TWV5-loaded fibers nanocomposites. (d) Dye photodegradation dynamics using MON-loaded fibers, under visible light excitation. The TiO_2 and TWV5 powders (with higher and lower bandgap, respectively) were also tested for comparison purposes. (e) Derivative of the relative concentration of RhB with time. (f) Application of the pseudo-first-order kinetic model to the experimental data.

Differently, the MON supported in the fibers showed photocatalytic activity under the action of visible light (using a lower energy $h\nu$). The dye degradation percentage achieved after 120 min of visible light irradiation were 73%, 75%, and 92%, using TW- to TWV5-containing fibers, respectively.

The derivative of the relative concentration of RhB with time $\left(\frac{d(C/C_0)}{dt}\right)$ (Figure 7e) showed that the greatest excursion in the rate of dye degradation, in the time interval of greatest decay of C, occurs with the use of fibers loaded with TWV5 nanostructures (followed by TWV3- and TW-loaded fibers samples, respectively), in a relationship directly proportional to the pollutant photodegradation kinetics.

For the studied metal oxide nanostructures, the RhB photodegradation kinetics was given in terms of the reaction rate coefficient (k), obtained from the application of the pseudo first order (PFO) model [48] to the experimental data. According to the model, k is equivalent to the value of the slope of the linear fit in the graph $\ln(C_0/C)$ versus t (Figure 7f). In fact, the dye degradation process is well-fitted by PFO kinetics, since the correlation constants for the three MON were close to 1 (best fit results).

The values obtained for the reaction rate coefficient were 1.92×10^{-2} , 1.98×10^{-2} , and $2.83 \times 10^{-2} \text{ min}^{-1}$, using the samples TW-, TWV3-, and TWV5-loaded fibers. In other words, it was proven that the highest reaction rate was obtained with the sample with the highest concentration of vanadium.

Especially, the increase in the doping level provided a decrease in the TiO_2 bandgap (as discussed previously). This allowed the occurrence of free electrons in the conduction band and holes in the valence band, essential to the dye degradation reactions in solution.

The TWV5 powder was also tested and returned a percentage of degradation similar to the noted for TW and TWV3 nanostructures dispersed in the fibers. This demonstrates that the performance difference between the TWV5 powder and fiber-supported TWV5 forms is associated to the greater surface area of these MON induced by the high level of nanoparticles dispersion in the electrospun fibers. More specifically, at the atomic level, vanadium ion substituents induce stress on the TiO_2 (host metal oxide) crystal structure. This configuration results in the formation of a large amount of defects in its crystal lattice, providing superior chemical reactivity for photocatalysis processes.

Based on the values of optical bandgap energies and photodegradation results, we present a possible photocatalytic mechanism for the RhB degradation in water, using the TWV5-loaded fibers nanocomposites (illustrated in Figure 8). The authors suggest that the larger surface area of the V-doped TiO_2/WO_3 (1/1 in mol) nanostructures (that is obtained with their dispersion in the fibers) induces more reactive sites for the photocatalytic reactions that occur on the surface of these semiconductors, promotes a lower probability of e^-/h^+ recombination, and enhances the charge transport [49]. In the illustrative scheme (Figure 8), the (V vs. NHE)-axis means the band potential versus normal hydrogen electrode scale [49]. The positions of the potentials of the TiO_2 and WO_3 band edges at pH 7.0 were given according to the literature [50]. Note that there is a difference in the edge positions of both oxides. This creates a potential gradient at the nanocomposite interface, which would facilitate the charge separation and inhibit the e^-/h^+ recombination [12,49,51].

The RhB photodegradation using TiO_2/WO_3 -based nanocomposites typically involves the action of the hydroxyl ($\bullet\text{OH}$) and superoxide ($\bullet\text{O}_2^-$) radicals [11,12,49,52]. The continuous incidence of visible light in the reactor environment generates available electrons and holes ($h\nu \rightarrow e^- + h^+$) in both WO_3 and V-doped TiO_2 oxides for the photocatalysis reactions.

Part of the photogenerated electrons also tend to be transferred from WO_3 to V-doped TiO_2 , due to the potential difference [53,54] (which is influenced by V donor levels below the TiO_2 CB, as previously discussed). Similarly, as the potential of the V-doped TiO_2 VB edge is more positive than that of WO_3 , it is suggested that the holes generated in the BV of the first oxide can also move into the BV of this last one. In summary, a hole can migrate to the semiconductor nanocomposite interface either directly or after their transfer from one oxide to another. These charge transfers in opposite directions can decrease recombination rates, in addition to promoting sufficient electron/hole separation for the photocatalysis

process to occur more efficiently [49,53]. Thus, the electrons and holes that reach the semiconductor-solution interface can react with the redox species O_2 and H_2O and form the superoxide ($\bullet O_2^-$, $O_2 + e^- \rightarrow \bullet O_2^-$) and hydroxyl ($\bullet OH$, $H_2O + h^+ \rightarrow \bullet OH$) radicals. The analysis of these processes indicates that these radicals and the photogenerated holes are the main agents of oxidation of the organic pollutant RhB into carbon dioxide and water. Thus, the best catalytic activity, obtained with TWV5-loaded fibers, stems from the combination of improved photoresponse and charge separation efficiency, and the presence of a higher active sites density of the hybrid nanostructures [55].

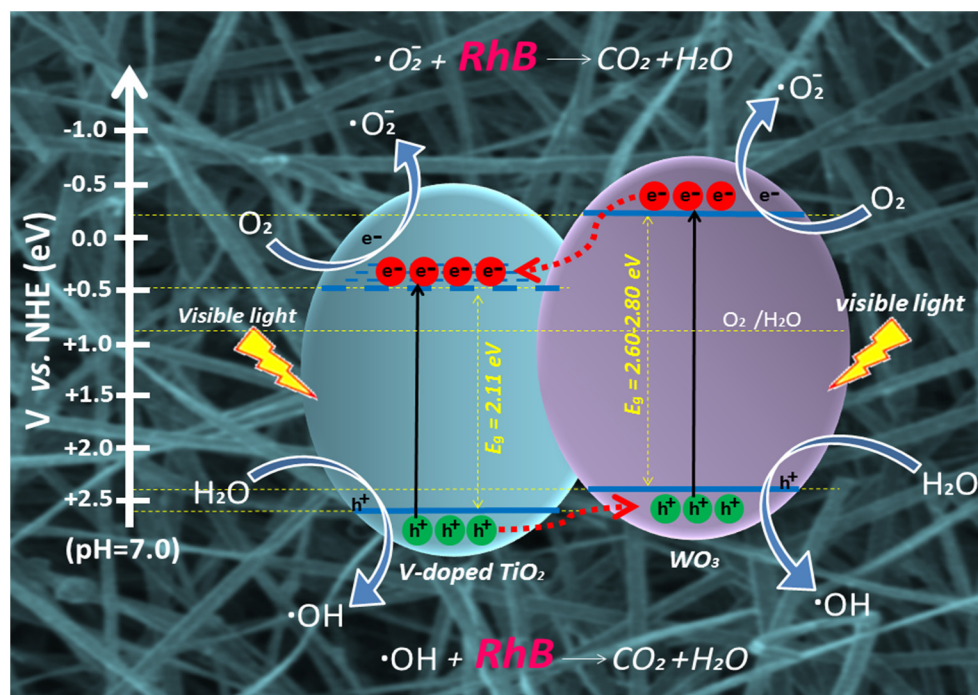


Figure 8. Possible photocatalytic mechanism for the RhB degradation in water, using the TWV5-loaded fibers nanocomposites.

Based on these aspects, the TWV5-loaded fibers were reused in two new photodegradation cycles (Figure 9). The second cycle (Figure 9b) returned a percentage of RB dye degradation of 90% after 120 min of radiation incidence. In the third cycle (Figure 9c), the percentage of 85% was obtained, and with a slight decrease in the reaction rate, with degradation saturation after 140 min of exposure of the material to white light.

The XRD spectrum of TWV5-loaded fibers (Figure 9d), after the third cycle of photodegradation, showed that all the characteristic peaks of TiO_2 and WO_3 (previously described in Figure 1) were preserved after the electrospinning processes and the photocatalysis cycles, with no phase change in the constituent oxides. It is important to highlight that the recyclability of the material is feasible due to the hydrophobic nature of the polymeric membrane and the maintenance of the MON photoactivity, without significant loss of the photocatalyst for reuse.

The photocatalysis process was discontinued with three cycles, since the polymer membrane showed imminence of mechanical wear (behavior expected by the acrylic nature of the polymer) caused by the handling and rearrangement of the material in the reactor during the preparation for its reuse.

In summary, the increasing level of vanadium doping in the crystalline structure of TiO_2 , the smaller bandgap value given to the TWV5 nanostructures, associated with their greater surface area when dispersed in electrospun fibers, prove the best results of dye degradation obtained with visible light.

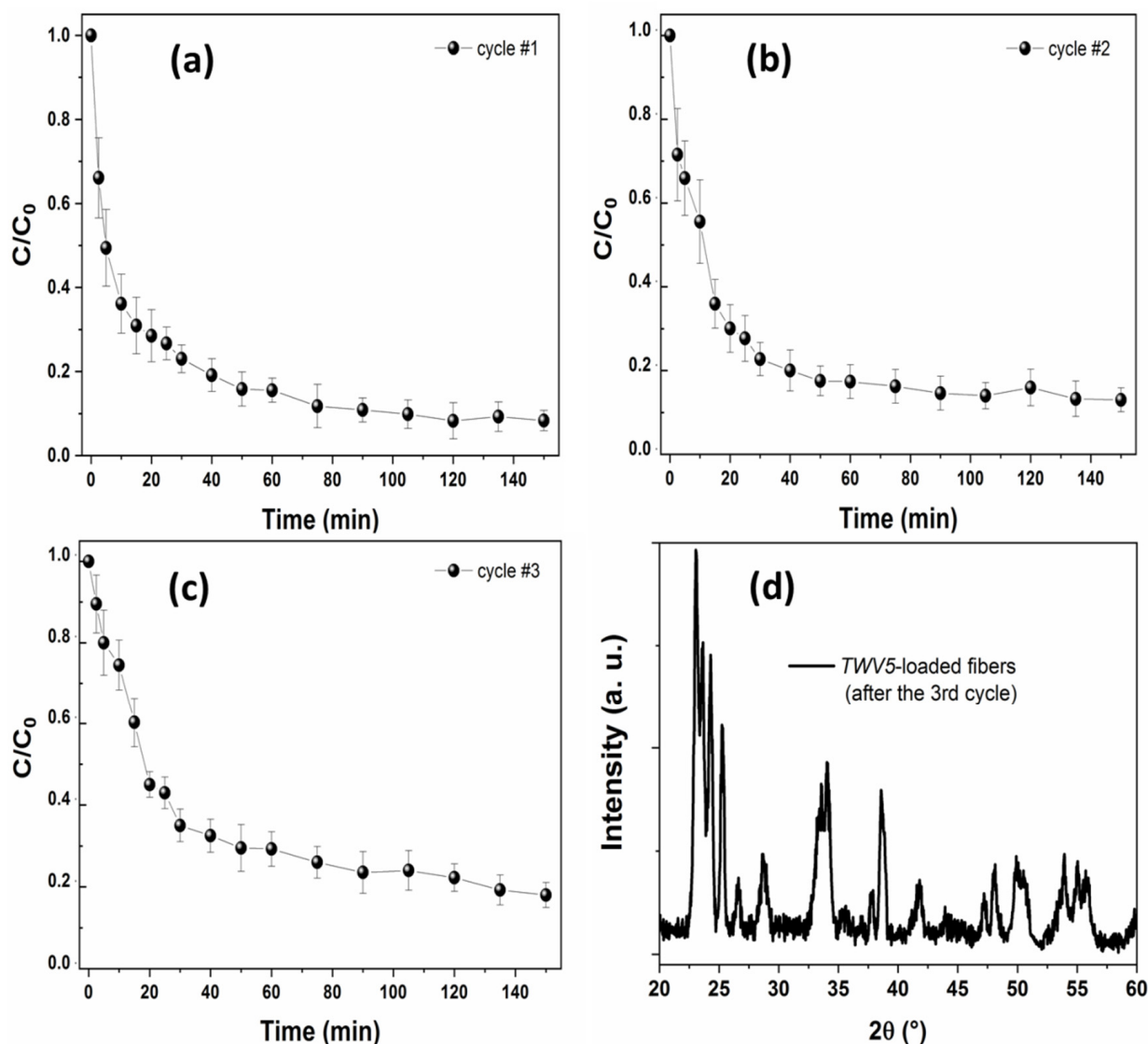


Figure 9. (a–c) Dye photodegradation cycles using TWV5-loaded fibers, under visible light excitation; (d) XRD spectrum of TWV5-loaded fibers, after the third cycle of photodegradation.

3. Materials and Methods

3.1. Materials

The chemicals titanium dioxide (anatase TiO_2 , 99.7% purity, <25 nm particle size, Sigma Aldrich, Burlington, VT, USA), tungsten trioxide (WO_3 , 99.9% purity, <100 nm particle size, Sigma Aldrich), vanadium pentoxide (V_2O_5 , 99.9% purity, 80 nm particle size, Nanoshell, Layton, UT, USA), acrylic copolymer Eudragit[®] L100 (Evonik Industries, Essen, NW, Germany), ethanol PA (99.8%, Neon Comercial, Suzano, Brazil), and rhodamine B (Vetec, São Paulo, SP, Brazil) were used as received. All these reagents are analytically pure.

3.2. Sample Preparation

The material samples for the photocatalysis tests were prepared in two steps: (i) sintering of metal oxide nanocomposites (MON) and (ii) dispersion of MON in electrospun polymeric membrane. The tested MON configurations were defined as: TiO_2/WO_3 (1/1 in mol, TW base sample); and TWV3 and TWV5 samples (TW mixture with 3 and 5 wt% of V_2O_5 , respectively).

For the sintering process, each metal oxide mixture was sintered in a muffle oven at 500 °C for 2 h [22]. For the electrospinning process, 0.25 g of each sintered MON was mechanically dispersed in 4 mL of alcoholic solution (with a polymer concentration of 0.27 g/mL) and inserted into the reservoir of a conventional syringe (volume of 10 mL and 0.7 mm of diameter of the metal needle). Thus, simultaneously, a pressure of 100 μLmin^{-1} on the syringe plunger and an electric potential difference (ddp) of 15 kV (applied to the tip of the metal capillary) promote the composite material to be electrospun towards a grounded plane metal collector (area of $0.1 \times 0.1 \text{ m}^2$, separated by 10 cm from the needle tip), with respective evaporation of the solvent. An illustration of the electrospinning process is shown in Figure 10a. The MON-contained fibrous membrane is then collected for the photocatalysis tests.

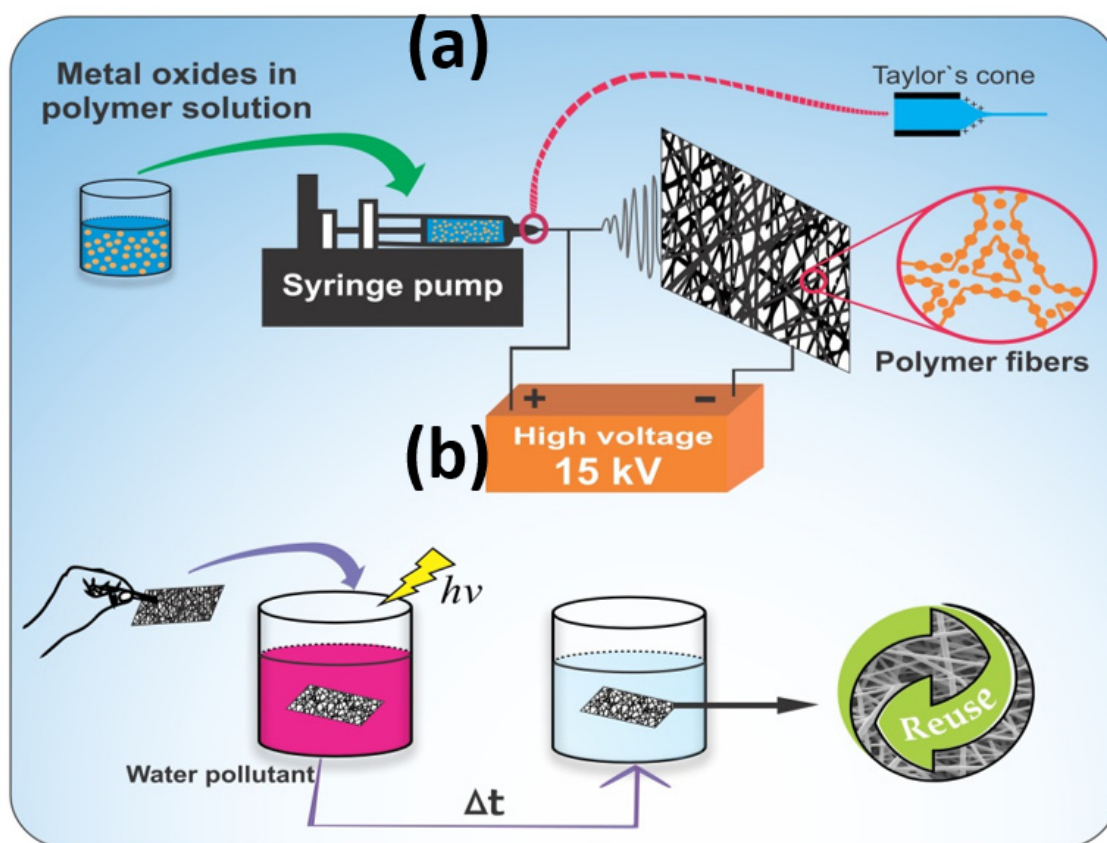


Figure 10. Illustrative scheme of the (a) MON dispersed in electrospun fibers and their use in (b) photodegradation of the dye in aqueous solution.

3.3. Microstructural Characterization

The sample microstructure was investigated by: scanning electron microscopy (SEM) and energy-dispersive X-ray spectroscopy (EDS) with 10 to 20 kV accelerating voltage (Vega 3XM Tescan equipment, Tescan, Brno, Czech Republic); X-ray diffraction (XRD) in the 20–60° range, scan rate of 0.02 °s⁻¹ and Cu K α radiation (Miniflex Rigaku equipment, Rigaku Corporation, Tokyo, Japan); Raman spectroscopy, excitation with $\lambda = 532 \text{ nm}$ laser, 20–25 mW (HORIBA Scientific, Osaka, Japan); differential scanning calorimetry (DSC), 30–300 °C range, nitrogen flow of 50 mL min⁻¹, heating temperature rate of 10 °C min⁻¹ (Schimadzu DSC-60 equipment, Shimadzu Corporation, Kyoto, Japan); and UV–vis with diffuse reflectance spectroscopy (DRS), 200–1400 nm wavelength range (Schimadzu UV-2600i spectrophotometer, Shimadzu Corporation, Kyoto, Japan).

3.4. Photocatalysis Tests

The temporal dynamics of the photocatalysis process was investigated from the variations in the UV-vis absorption of Rhodamine B dye (peak centered at 555 nm) solution (neutral pH) (on a Hach DR 5000 UV-vis spectrophotometer, Hach Company, Ames, IA, USA), under the action of the MON-loaded fibers (19 mg) (scheme in Figure 10b). The photocatalysis tests were performed in a closed cubic box (volume of 40 cm³), equipped with lateral heat dissipating fans, reactor (capacity of 150 mL, placed on a magnetic stirrer and connected to a sample collection system), and light source (Figure 11a). The metal oxide nanostructures were activated by continuous white light (60 W power, 650 lm/m² intensity, spectrum in Figure 11b). The solution in the reactor (surface top) was maintained at 16.5 cm from the light source end. The reuse of composites in new photocatalysis cycles was possible by washing the material in aqueous solution (ultrapure water, neutral pH) under constant agitation for 3 h followed by drying in an oven at 40 °C for 12 h. All measurements were made in triplicate.

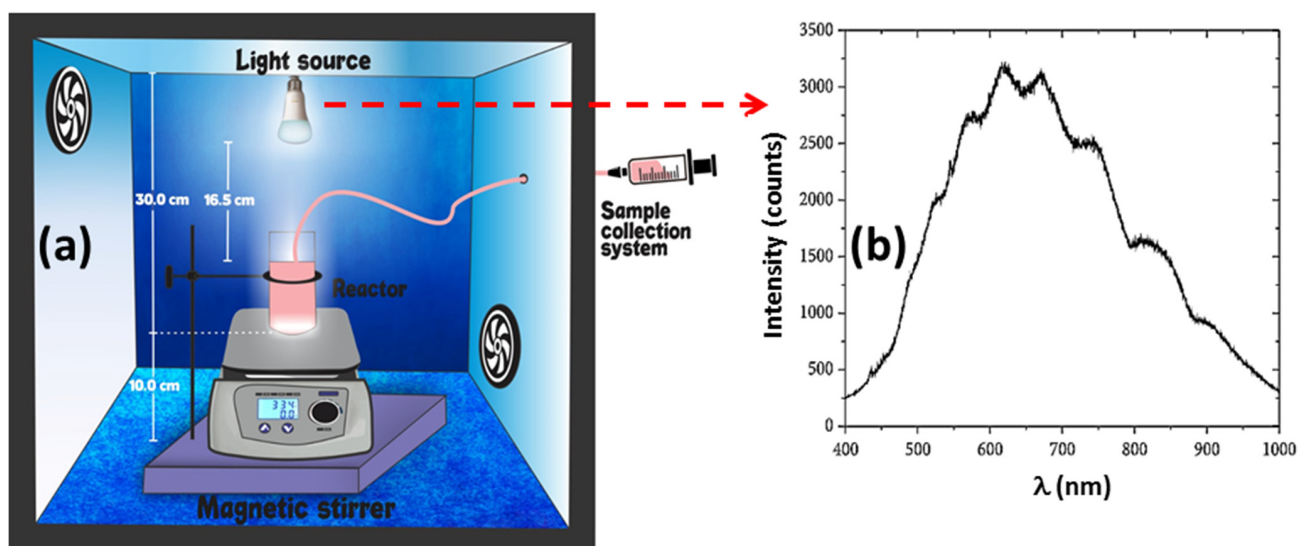


Figure 11. (a) Experimental apparatus for photocatalysis tests; (b) emission spectrum of white light applied during the photocatalysis experiments.

3.5. Statistical Analysis

The particles size, fibers diameter, and temporal dynamics of the dye photodegradation were given as an average of three independent measurements for each tested MON configuration. The normality and equality of means tests (95% confidence level, comparing the significance level (α) to the p-value returned by statistical tests) were performed as population statistics. The sample sizes (n) were obtained from SEM images using ImageJ software (National Institutes of Health, Bethesda, MD, USA).

4. Conclusions

The main aim of the current research was to investigate the preparation of vanadium-doped TiO₂/WO₃ nanostructures supported on electrospun membranes, their microstructural characterization, and their potential application as photocatalysts. The planned MON-loaded fibers were successfully produced from the sintering and electrospinning processes. All composites showed photocatalytic activity in visible light, with better performance for the sample with 5 wt% of V₂O₅.

The saturation in the unit cell volume and crystallite size of TiO₂, from the TWV3 to TWV5 sample, and the doping of TiO₂ (observed in the microstructural characterization) confirm that the best results of dye photodegradation, anoted for the TWV5-loaded fibers, are directly influenced by the higher doping level of V⁵⁺ ions in this system.

In addition, the use of polymer matrix as a support for metal oxide nanostructures allowed the production of flexible devices, provided better photocatalytic performance of oxides and ease of removal of oxides from the aqueous environment, without significant loss of photocatalyst for reuse.

Based on the excellent results of photocatalysis using TWV5 nanostructures, the continuity of research involves the execution of other important experiments to quantify parameters of the photodegradation mechanism of RhB (and other dyes) using these metal oxide nanocomposites, such as active species trapping and transient photocurrent test (evaluating the separation efficiency of charge carriers over the photocatalyst surface). Other perspectives involve the use of selective oxides as dopants (for example, Nb₂O₅, MoO₃ and In₂O₃); the improvement of the mechanical strength properties of the polymeric membrane that supports the MON nanostructures; development of the mechanical support apparatus for tests with the photocatalyst in an environment with larger proportions; and use of these nanostructured devices in other chemical decontamination processes.

Author Contributions: Sample preparation and characterization, M.F.G.P., M.M.N., P.H.N.C., C.Y.B.O., G.F.T. and E.S.A. Writing, editing, and review, M.F.G.P., C.Y.B.O. and E.S.A. All authors have read and agreed to the published version of the manuscript.

Funding: This research was funded by Conselho Nacional de Desenvolvimento Científico e Tecnológico (CNPq, Project 202451/2015-1), Fundação de Amparo à Pesquisa do Estado da Bahia (FAPESB, Project 1252/2018) and Fundação de Amparo a Ciência e Tecnologia do Estado de Pernambuco (FACEPE, project IBPG-0849-3.03/2020) Brazilian research agencies.

Institutional Review Board Statement: Not applicable.

Informed Consent Statement: Not applicable.

Data Availability Statement: Not applicable.

Conflicts of Interest: The authors declare no conflict of interest.

References

1. Handojo, L.; Ikhsan, N.A.; Mukti, R.R.; Indarto, A. Nanotechnology for remediations of agrochemicals. In *Agrochemicals Detection, Treatment and Remediation*; Narasimha, M., Prasad, V., Eds.; Butterworth-Heinemann: London, UK, 2020; pp. 535–567.
2. Li, X.; Yu, J.; Jiang, C. Principle and surface science of photocatalysis. *Interface Sci. Technol.* **2020**, *31*, 1–38.
3. Kwaadsteniet, M.; Dobrowsky, P.; Deventer, A.V.; Khan, W.; Cloete, T. Domestic rainwater harvesting: Microbial and chemical water quality and point-of-use treatment systems. *Water Air Soil Pollut.* **2013**, *224*, 1629–1637. [[CrossRef](#)]
4. Presura, E.; Robescu, L. Energy use and carbon footprint for potable water and wastewater treatment. *Proc. Int. Conf. Bus. Excell.* **2017**, *11*, 191–198. [[CrossRef](#)]
5. Chen, J.; Luo, J.; Luo, Q.; Pang, Z. *Wastewater Treatment*; De Gruyter: Berlin, Germany; Boston, MA, USA, 2018.
6. Moga, I.C.; Ardelean, I.; Donțu, O.G.; Moisesescu, C.; Băran, N.; Petrescu, G.; Voicea, I. Materials and Technologies Used in Wastewater Treatment. *IOP Conf. Ser. Mater. Sci. Eng.* **2018**, *374*, 012079. [[CrossRef](#)]
7. Carolin, C.F.; Kumar, P.S.; Saravanan, A.; Joshiba, G.J.; Naushad, M. Efficient techniques for the removal of toxic heavy metals from aquatic environment: A review. *J. Environ. Chem. Eng.* **2017**, *5*, 2782–2799. [[CrossRef](#)]
8. Yaqoob, A.A.; Parveen, T.; Umar, K.; Ibrahim, M.N.M. Role of Nanomaterials in the Treatment of Wastewater: A Review. *Water Sci. Eng.* **2020**, *12*, 495. [[CrossRef](#)]
9. Ganachari, S.V.; Hublikar, L.; Yaradoddi, J.S.; Math, S.S. Metal oxide nanomaterials for environmental applications. In *Handbook of Ecomaterials*; Martínez, L., Kharissova, O., Kharisov, B., Eds.; Springer: Singapore, 2019; pp. 2357–2368.
10. Yang, Y.; Niu, S.; Han, D.; Liu, T.; Wang, G.; Li, Y. Progress in Developing Metal Oxide Nanomaterials for Photoelectrochemical Water Splitting. *Adv. Energy Mater.* **2017**, *7*, 170–555. [[CrossRef](#)]
11. Choi, T.; Kim, J.S.; Kim, J.H. Transparent nitrogen doped TiO₂/WO₃ composite films for self-cleaning glass applications with improved photodegradation activity. *Adv. Powder Technol.* **2016**, *27*, 347–353. [[CrossRef](#)]
12. Baia, L.; Orbán, E.; Fodor, S.; Hampel, B.; Kedves, E.Z.; Székely, I.; Pap, Z. Preparation of TiO₂/WO₃ composite photocatalysts by the adjustment of the semiconductors' surface charge. *Mater. Sci. Semicond. Processing* **2016**, *42*, 66–71. [[CrossRef](#)]
13. Ibhaddon, A.O.; Fitzpatrick, P. Heterogeneous Photocatalysis: Recent Advances and Applications. *Catalysts* **2013**, *3*, 189–218. [[CrossRef](#)]
14. Wang, H.; Li, X.; Zhao, X.; Li, C.; Song, X.; Zhang, P.; Huo, P. A review on heterogeneous photocatalysis for environmental remediation: From semiconductors to modification strategies. *Chin. J. Catal.* **2022**, *43*, 178–214. [[CrossRef](#)]

15. Upadhyay, G.K.; Rajput, J.K.; Pathak, T.K.; Kumar, V.; Purohit, L.P. Synthesis of ZnO: TiO₂ nanocomposites for photocatalyst application in visible light. *Vacuum* **2019**, *160*, 154–163. [[CrossRef](#)]
16. Caswell, T.; Dlamini, M.W.; Miedziak, P.J.; Pattison, S.; Davies, P.R.; Taylor, S.H.; Hutchings, G.J. Enhancement in the rate of nitrate degradation on Au-and Ag-decorated TiO₂ photocatalysts. *Catal. Sci. Technol.* **2020**, *10*, 2082–2091. [[CrossRef](#)]
17. Xu, W.; Shu, G.; Zhang, S.; Song, L.; Ma, K.; Yue, H. In-Situ Fabricating V₂O₅/TiO₂-Carbon Heterojunction from Ti₃C₂ MXene as Highly Active Visible-Light Photocatalyst. *J. Nanomater.* **2022**, *12*, 1776. [[CrossRef](#)] [[PubMed](#)]
18. Julkapli, N.M.; Bagheri, S.; Yousefi, A.T. TiO₂ Hybrid Photocatalytic Systems: Impact of Adsorption and Photocatalytic Performance. *Rev. Inorg. Chem.* **2015**, *35*, 151–178.
19. Kadam, A.V. Propylene glycol-assisted seed layer-free hydrothermal synthesis of nanostructured WO₃ thin films for electrochromic applications. *J. Appl. Electrochem.* **2017**, *47*, 335–342. [[CrossRef](#)]
20. Qi, J.J.; Gao, S.; Chen, K.; Yang, J.; Zhao, H.W.; Guo, L.; Yang, S.H. Vertically aligned, double-sided, and self-supported 3D WO₃ nanocolumn bundles for low-temperature gas sensing. *J. Mater. Chem.* **2015**, *7*, 10108–10114. [[CrossRef](#)]
21. Zhang, Q.; Wu, Y.; Li, L.; Zuo, T. Sustainable Approach for Spent V₂O₅-WO₃/TiO₂ Catalysts Management: Selective Recovery of Heavy Metal Vanadium and Production of Value-Added WO₃-TiO₂ Photocatalysts. *ACS Sustain. Chem. Eng.* **2018**, *6*, 12502–12510. [[CrossRef](#)]
22. Araújo, E.S.; Leão, V.N.S. TiO₂:WO₃ heterogeneous structures prepared by electrospinning and sintering steps: Characterization and analysis of the impedance variation to humidity. *J. Adv. Ceram.* **2019**, *8*, 238–246. [[CrossRef](#)]
23. Yan, J.; Wu, G.; Guan, N.; Li, L. Nb₂O₅/TiO₂ Heterojunctions: Synthesis Strategy and Photocatalytic Activity. *Appl. Catal.* **2014**, *152*, 280–288. [[CrossRef](#)]
24. Mandal, R.K.; Kundu, S.; Sain, S.; Pradhan, S.K. Enhanced photocatalytic performance of V₂O₅-TiO₂ nanocomposites synthesized by mechanical alloying with morphological hierarchy. *New J. Chem.* **2019**, *43*, 2804–2816. [[CrossRef](#)]
25. Chen, M.; Wei, X.; Liang, J.; Li, S.; Zhang, Z.; Tang, F. Effects of CrO_x species doping on V₂O₅-WO₃/TiO₂ catalysts on selective catalytic reduction of NO_x by NH₃ at low temperature. *Reac. Kinet. Mech. Cat.* **2022**, *135*, 1767–1783. [[CrossRef](#)]
26. Wu, Z.; Chen, H.; Wan, Z.; Zhang, S.; Zeng, Y.; Guo, H.; Zhong, Q.; Li, X.; Han, J.; Rong, W. Promotional Effect of S Doping on V₂O₅-WO₃/TiO₂ Catalysts for Low-Temperature NO_x Reduction with NH₃. *Ind. Eng. Chem. Res.* **2020**, *59*, 15478–15488. [[CrossRef](#)]
27. Hiemstra, T. Formation, stability, and solubility of metal oxide nanoparticles: Surface entropy, enthalpy, and free energy of ferrihydrite. *Geochim. Cosmochim. Acta* **2015**, *158*, 179–198. [[CrossRef](#)]
28. Tanev, P.; Chibwe, M.; Pinnavaia, T. Titanium-containing mesoporous molecular sieves for catalytic oxidation of aromatic compounds. *Nature* **1994**, *368*, 321–323. [[CrossRef](#)]
29. Lee, D.W.; Yoo, B.R. Advanced metal oxide (supported) catalysts: Synthesis and applications. *Ind. Eng. Chem. Res.* **2014**, *20*, 3947–3959. [[CrossRef](#)]
30. Fatimah, I.; Fadillah, G.; Yanti, I.; Doong, R. Clay-Supported Metal Oxide Nanoparticles in Catalytic Advanced Oxidation Processes: A Review. *J. Nanomater.* **2022**, *12*, 825. [[CrossRef](#)]
31. Araújo, E.S.; da Costa, B.P.; Oliveira, R.A.P.; Libardi, J.; Faia, P.M.; de Oliveira, H.P. TiO₂/ZnO hierarchical heteronanostructures: Synthesis, characterization and application as photocatalysts. *J. Environ. Chem. Eng.* **2016**, *4*, 2820–2829. [[CrossRef](#)]
32. Treacy, J.P.; Hussain, H.; Torrelles, X.; Grinter, D.C.; Cabailh, G.; Bikondoa, O.; Thornton, G. Geometric structure of anatase TiO₂(101). *Phys. Rev. B* **2017**, *95*, 075–416. [[CrossRef](#)]
33. Leng, X.; Pereiro, J.; Strle, J.; Bollinger, A.T.; Božović, I. Epitaxial growth of high quality WO₃ thin films. *APL Mater.* **2015**, *3*, 096–102. [[CrossRef](#)]
34. Faia, P.M.; Libardi, J.; Louro, C.S. Effect of V₂O₅ doping on P- to N-conduction type transition of TiO₂:WO₃ composite humidity sensors. *Sens. Actuators B Chem.* **2016**, *222*, 952–964. [[CrossRef](#)]
35. Chen, A.; Li, C.; Zhang, C.; Li, W.; Yang, Q. The mechanical hybrid of V₂O₅ microspheres/graphene as an excellent cathode for lithium-ion batteries. *J. Solid. State Electrochem.* **2022**, *26*, 729–738. [[CrossRef](#)]
36. Kniec, K.; Ledwa, K.; Marciniak, L. Enhancing the Relative Sensitivity of V⁵⁺, V⁴⁺ and V³⁺ Based Luminescent Thermometer by the Optimization of the Stoichiometry of Y₃Al₅-xGa_xO₁₂ Nanocrystals. *Nanomaterials* **2019**, *9*, 1375. [[CrossRef](#)] [[PubMed](#)]
37. Lima, F.M.; Martins, F.M.; Maia Júnior, P.H.F.; Almeida, A.F.L.; Freire, F.N. Nanostructured titanium dioxide average size from alternative analysis of Scherrer's Equation. *Matéria* **2018**, *23*, 1–9. [[CrossRef](#)]
38. Miranda, M.A.R.; Sasaki, J.M. The limit of application of the Scherrer equation. *Acta Crystallogr. A Found. Adv.* **2018**, *74*, 54–65. [[CrossRef](#)]
39. Sahoo, S.; Arora, A.K.; Sridharan, V. Raman line shapes of optical phonons of different symmetries in anatase TiO₂ nanocrystals. *J. Phys. Chem. C* **2009**, *113*, 16927–16933. [[CrossRef](#)]
40. Su, C.Y.; Lin, H.C.; Lin, C.K. Fabrication and optical properties of Ti-doped W₁₈O₄₉ nanorods using a modified plasma-arc gas-condensation technique. *J. Vac. Sci. Technol. B* **2009**, *27*, 2170–2174. [[CrossRef](#)]
41. Yang, C.C.; Li, S. Size-dependent Raman red shifts of semiconductor nanocrystals. *J. Phys. Chem. B* **2008**, *112*, 14193–14197. [[CrossRef](#)]
42. Sangeetha, P.; Jayapandi, S.; Saranya, C.; Ramakrishnan, V. Phonon confinement and size effect in Raman spectra of TiO₂ nanocrystal towards Photocatalysis Application. *J. Aust. Ceram. Soc.* **2021**, *57*, 533–541. [[CrossRef](#)]

43. Tan, Z.; Sato, K.; Ohara, S. Synthesis of layered nanostructured TiO₂ by hydrothermal method. *Adv. Powder Technol.* **2015**, *26*, 296–302. [[CrossRef](#)]
44. Patrycja Makuła, P.; Pacia, M.; Macyk, W. How to correctly determine the band gap energy of modified semiconductor photocatalysts Based on UV–Vis Spectra. *J. Phys. Chem. Lett.* **2018**, *9*, 6814–6817. [[CrossRef](#)] [[PubMed](#)]
45. Illangakoon, U.E.; Nazir, T.; Williams, G.R.; Chatterton, N.P. Mebeverinloaded electrospun nanofibers: Physicochemical characterization and dissolution studies. *J. Pharm. Sci.* **2014**, *103*, 283–292. [[CrossRef](#)] [[PubMed](#)]
46. Franco, P.; De Marco, I. Eudragit: A Novel Carrier for Controlled Drug Delivery in Supercritical Antisolvent Coprecipitation. *Polymers* **2020**, *12*, 234. [[CrossRef](#)] [[PubMed](#)]
47. Kishori, L.D.; Nilima, A.T.; Gide, P.S. Formulation and development of tinidazole microspheres for colon targeted drug delivery system. *J. Pharm. Res.* **2013**, *6*, 158–165.
48. Revellame, E.D.; Fortela, D.L.; Sharp, W.; Hernandez, R.; Zappi, M.E. Adsorption kinetic modeling using pseudo-first order and pseudo-second order rate laws: A review. *Clean. Eng. Technol.* **2020**, *1*, 100032. [[CrossRef](#)]
49. Luo, X.; Liu, F.; Li, X.; Gao, H.; Liu, G. WO₃/TiO₂ nanocomposites: Salt-ultrasonic assisted hydrothermal synthesis and enhanced photocatalytic activity. *Mater. Sci. Semicond. Processing* **2013**, *16*, 1613–1618. [[CrossRef](#)]
50. Bledowski, M.; Wang, L.; Ramakrishnan, A.; Khavryuchenko, O.V.; Khavryuchenko, V.D.; Ricci, P.C.; Beranek, R. Visible-light photocurrent response of TiO₂–polyheptazine hybrids: Evidence for interfacial charge-transfer absorption. *Phys. Chem. Chem. Phys.* **2011**, *13*, 21511–21519. [[CrossRef](#)]
51. Lee, W.H.; Lai, C.W.; Abd Hamid, S.B. One-step formation of WO₃-loaded TiO₂ nanotubes composite film for high photocatalytic performance. *Materials* **2015**, *8*, 2139–2153. [[CrossRef](#)]
52. Gao, L.; Gan, W.; Qiu, Z.; Zhan, X.; Qiang, T.; Li, J. Preparation of heterostructured WO₃/TiO₂ cat-alysts from wood fibers and its versatile photodegradation abilities. *Sci. Rep.* **2017**, *7*, 1102. [[CrossRef](#)]
53. Enesca, A. The Influence of Photocatalytic Reactors Design and Operating Parameters on the Wastewater Organic Pollutants Removal—A Mini-Review. *Catalysts* **2021**, *11*, 556. [[CrossRef](#)]
54. Huang, Z.F.; Zou, J.J.; Pan, L.; Wang, S.; Zhang, X.; Wang, L. Synergetic promotion on photoactivity and stability of W18O₄₉/TiO₂ hybrid. *Appl. Catal. B-Environ.* **2014**, *147*, 167–174. [[CrossRef](#)]
55. Luo, X.; He, G.; Fang, Y.; Xu, Y. Nickel sulfide/graphitic carbon nitride/strontium titanate (NiS/g-C₃N₄/SrTiO₃) composites with significantly enhanced photocatalytic hydrogen production activity. *J. Colloid. Interface Sci.* **2018**, *518*, 184–191. [[CrossRef](#)] [[PubMed](#)]